RSC Advances

PAPER

View Article Online
View Journal | View Issue

Cite this: *RSC Adv.*, 2025, **15**, 49652

First-principles investigation of the optical and piezoelectric properties of Janus TiOS monolayers

Jing Tang,[a] Kaimin Fan *[b] and Kun Wang[c]

Using first-principles calculations, we systematically explore the geometric structures, stabilities, electronic structures, optical responses, and piezoelectric properties of Janus TiOS monolayers to assess their suitability for integrated photocatalytic and piezoelectric applications. The stability of both phases was assessed through formation energy calculations, phonon dispersion relations, AIMD simulations, and elastic constant analyses, which collectively confirm their dynamical, thermal, and mechanical stability. Electronic structure calculations reveal that the 1T-TiOS monolayer is a direct-band-gap semiconductor (E_g = 1.27 eV), whereas the 2H phase exhibits an indirect band gap of 1.52 eV. Charge-density analyses indicate that the CBM is mainly contributed by Ti 3d orbitals, while the VBM originates from S 2p states, providing a favourable orbital configuration for efficient charge separation. Both phases exhibit strong visible-light absorption, with absorption coefficients exceeding 1 × 10^5 cm^{-1}. Remarkably, the 1T- and 2H-TiOS monolayers demonstrate strong potential as solar-driven photocatalysts for water splitting over a broad pH range (0–10). Furthermore, Janus TiOS monolayers show intrinsic and pronounced piezoelectric responses. For the 1T phase, the in-plane and out-of-plane piezoelectric coefficients are 4.99 and 0.32 pm V^{-1}, respectively, while the corresponding values for the 2H phase are 2.38 and 0.27 pm V^{-1}. These results indicate that Janus TiOS monolayers are promising candidates for next-generation materials integrating photocatalytic and piezoelectric functionalities.

Received 17th October 2025
Accepted 6th December 2025

DOI: 10.1039/d5ra07953e

rsc.li/rsc-advances

1 Introduction

The rutile and anatase phases of TiO_2 have been extensively employed in photocatalytic and electrochemical applications owing to their non-toxicity, low cost, and excellent stability.[1,2] However, bulk TiO_2 suffers from several intrinsic drawbacks, including a relatively small surface area, which limits the number of active sites, and a high recombination rate of photogenerated charge carriers (electrons and holes), thereby reducing catalytic efficiency.[3–5] In addition, its wide band gap (3.0–3.2 eV) restricts absorption to the ultraviolet region of the solar spectrum.[6] To overcome these limitations, researchers have explored the transformation of TiO_2 structures from the bulk to the two-dimensional (2D) scale.[7,8] This transition aims to enhance the surface area through a layered structure, shorten the diffusion path of charge carriers, and improve photocatalytic efficiency. Recent studies have shown that 2D TiO_2 can exist in several phases, including 1T (octahedral), 2H (hexagonal), LNS (lepidocrocite), ANS (anatase), and HNS (hexagonal nanosheet). Among these, the 1T phase, which can be exfoliated from hexagonal $NaTiO_2$, exhibits a low effective hole mass but still possesses a relatively large band gap of 3.29 eV.[9] The band gaps of 1T- and 2H-TiO_2 monolayers are calculated to be 3.72 eV and 5.74 eV, respectively, as reported by Rasmussen *et al.*[10] These results demonstrate that wide band gaps are an inherent characteristic of 2D TiO_2, which fundamentally limits its photocatalytic applications.

Recently, Janus 2D materials have attracted considerable attention as a novel class of layered materials.[11–14] Distinct from conventional symmetric 2D structures, these materials exhibit mirror asymmetry and possess an intrinsic vertical dipole moment, which enhances charge-carrier separation and makes them a highly promising platform for high-performance photocatalytic and piezoelectric applications.[15,16] Representative examples include Janus MoSSe and WSSe, where the electronegativity difference across the asymmetric surfaces gives rise to unique optical and catalytic properties that surpass those of their symmetric counterparts, MoS_2 and WS_2.[17–19] Dong *et al.* demonstrated that Janus MXY monolayers (M = Mo or W; X/Y = S, Se, or Te) generate strong in-plane and weak out-of-plane piezoelectric polarizations under uniaxial strain.[20] Moreover, the successful synthesis of Janus MoSSe and WSSe monolayers has confirmed their experimental feasibility.[21,22] Inspired by these advances, Ti-based Janus materials have also attracted increasing attention. Mogulkoc *et al.* investigated the structural, mechanical, electronic, thermal, and optical properties of TiXY

[a]*School of Ecology and Environmental Science, Qinghai Institute of Technology, Xining 810016, China*

[b]*Center for General Education, Qinghai Institute of Technology, Xining 810016, China. E-mail: fankm128@163.com*

[c]*Xingzhi College, Zhejiang Normal University, Jinhua 321004, China*

(X/Y = S, Se, and Te) monolayers using first-principles calculations.[23] Yang *et al.* reported that Janus TiXY (X ≠ Y; X/Y = Cl, Br, I) monolayers exhibit thermal, dynamical, and mechanical stability, together with outstanding in-plane and out-of-plane piezoelectric responses.[16] Similarly, Yan *et al.* found that TiPX (X = F, Cl, Br) monolayers are dynamically and mechanically stable, possess high carrier mobility, and display remarkable flexibility and piezoelectricity.[24]

Motivated by the exceptional performance of Janus materials, we designed Janus TiOS monolayers derived from the 1T and 2H phases of TiO_2 by replacing the oxygen layer on one side with sulfur to form an asymmetric structure. The larger atomic radius and shallower p-orbital energy levels of sulfur effectively narrow the band gap and enhance visible-light absorption. Furthermore, the electronegativity difference between the oxygen and sulfur layers induces vertical polarization, facilitating efficient electron–hole separation. In this work, we systematically explore the electronic, optical, mechanical, and piezoelectric properties of Janus TiOS monolayers using first-principles calculations. The results reveal that Janus TiOS not only mitigates the optical and electronic limitations of 2D TiO_2 but also exhibits distinct advantages for photocatalysis and piezoelectric applications, providing theoretical guidance for the development of high-performance Ti-based 2D materials.

2 Computational methods

All first-principles calculations in this study were performed within the framework of density functional theory (DFT) using the Vienna *Ab initio* Simulation Package (VASP).[25,26] The interactions between valence electrons and ionic cores were described by the projector-augmented wave (PAW) method.[27,28] To account for van der Waals interactions, the DFT-D3 correction proposed by Grimme was included.[29] A plane-wave cutoff energy of 500 eV was adopted, and a vacuum layer of 20 Å was added to eliminate spurious interlayer interactions. The convergence thresholds for energy and forces were set to 10^{-8} eV and 0.001 eV $Å^{-1}$, respectively. Geometry optimizations were carried out using the Perdew–Burke–Ernzerhof (PBE) functional within the generalized gradient approximation (GGA).[30] The Heyd–Scuseria–Ernzerhof hybrid functional (HSE06) was further employed to obtain more accurate electronic band structures.[31] A Monkhorst–Pack[32] *k*-point mesh of 10 × 10 × 1 was used for structural optimization, while a denser grid of 20 × 20 × 1 was adopted for the calculations of elastic moduli and piezoelectric coefficients. Phonon dispersion curves were calculated using density functional perturbation theory (DFPT) based on a 4 × 4 × 1 supercell (48 atoms) constructed with the Phonopy package.[33] *Ab initio* molecular dynamics (AIMD) simulations were performed at 300 K for 8 ps with a time step of 2.0 fs under the NVT ensemble.[34] The atomic structures were visualized and analyzed using the VESTA code.[35] The post-processing of calculation data was carried out using VASPKIT.[36]

3 Results and discussion

3.1 Structure and stability

The TiOS monolayers adopt a three-layered structure consisting of Ti, O, and S atomic planes, similar to the TiO_2 monolayers in the 1T and 2H phases, as shown in Fig. 1(a) and (b). They can be regarded as TiO_2 monolayers in which the top-layer O atoms are replaced by S atoms. The optimized structural parameters are listed in Table 1. The lattice constant (a), Ti–O and Ti–S bond lengths (d_{Ti-O} and d_{Ti-S}), and monolayer thickness (h) are found to be in good agreement with previously reported values.[37–39] Pronounced differences in the Ti–O and Ti–S bond lengths, as well as in the Ti–O–Ti and Ti–S–Ti bond angles, indicate the structural asymmetry of Janus TiOS monolayers. This asymmetry arises from the distinct atomic radii and electro negativities of O and S.

In addition, the formation energies of the two-phase Janus TiOS monolayers were calculated to evaluate their feasibility for experimental synthesis using the following formula:[39]

$$E_f = [E_{TiOS} - (E_{TiS_2} - E_S + E_O)]/n \quad (1)$$

where E_{TiOS} and E_{TiS_2} represent the energies of the Janus TiOS and TiS_2 monolayers, respectively. E_S is obtained from the energy of bulk sulfur divided by the number of atoms in its unit cell. $E_O = 1/2E_{O_2}$, where E_{O_2} denotes the energy of an oxygen molecule. The parameter n ($n = 3$) is the number of atoms in the unit cell. Our results show that all calculated E_f values are negative (Table 1), indicating that both TiOS phases are exothermic and experimentally feasible, similar to the Janus MoSSe monolayer synthesized by selectively replacing the top Se layer with S atoms.[40]

The phonon dispersion curves presented in Fig. 2(a) show the dynamical stability of Janus TiOS monolayers. Apart from a slight imaginary frequency near the Gamma point, no imaginary modes are present, indicating that both 1T- and 2H-TiOS

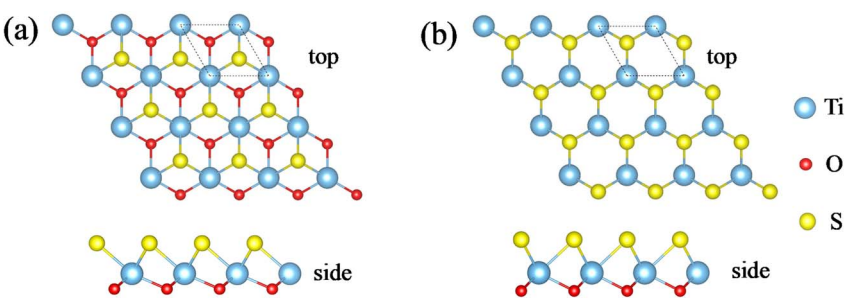

Fig. 1 Top and side views of (a) 1T- and (b) 2H-TiOS monolayers, with the unit cell marked by a black parallelogram.

Table 1 Structural parameters and electronic properties of Janus TiOS monolayers, including lattice constants (a), bond length (d), monolayer thickness (h), bond angles ($\angle$), formation energy (E_f), and band gaps obtained using the PBE and HSE06 functionals

Material	a (Å)	d_{Ti-O} (Å)	d_{Ti-S} (Å)	h (Å)	$\angle_{Ti-O-Ti}$ (°)	$\angle_{Ti-S-Ti}$ (°)	E_f (eV)	E_g^{PBE} (eV)	E_g^{HSE06} (eV)
1T-TiOS	3.18	2.00	2.43	2.39	105.12	81.67	−0.95	0.55	1.27
2H-TiOS	3.08	2.00	2.45	2.59	100.91	78.20	−0.88	0.62	1.52

monolayers are dynamically stable.[41] The thermodynamic stability was further evaluated by AIMD simulations. As illustrated in Fig. 2(b), the AIMD simulations performed at 300 K for 8 ps showed only minor energy fluctuations, while the overall lattice structures remained intact without any bond rupture or noticeable distortion. These results indicate that both monolayers are thermally stable at room temperature.[42]

To further elucidate the bonding characteristics, the electron localization function (ELF) was calculated, as shown in Fig. 3(a). The ELF distributions reveal that electrons are mainly localized around O and S atoms, whereas very little electron density is found between Ti and O/S atoms, indicating the predominantly ionic nature of the Ti–O and Ti–S bonds.[43] Moreover, the planar-averaged and 3D charge density differences of 1T- and 2H-TiOS monolayers, shown in Fig. 3(b), display clear electron depletion around the Ti sites and electron accumulation near the electronegative O and S atoms. This charge redistribution is consistent with the ELF analysis and provides further evidence for the predominantly ionic character of the Ti–O and Ti–S bonds. This observation is consistent with previous theoretical and experimental results.[44,45]

3.2 Electronic properties

In this section, the electronic properties of 1T- and 2H-TiOS monolayers are investigated using DFT calculations. The band structure analysis, as illustrated in Fig. 4(a)–(d), reveals distinct differences between the two phases. The 1T-TiOS monolayer exhibits a direct bandgap, where the conduction band minimum (CBM) is primarily derived from Ti atoms, and the valence band maximum (VBM) is predominantly contributed by S atoms. In contrast, the 2H-TiOS monolayer possesses an indirect bandgap. Its CBM is also dominated by Ti states, whereas the VBM is primarily composed of S states with a minor contribution from Ti. The calculated band gaps, as summarized in Table 1, demonstrate noticeable variations depending on the computational methods employed. Specifically, the 1T phase

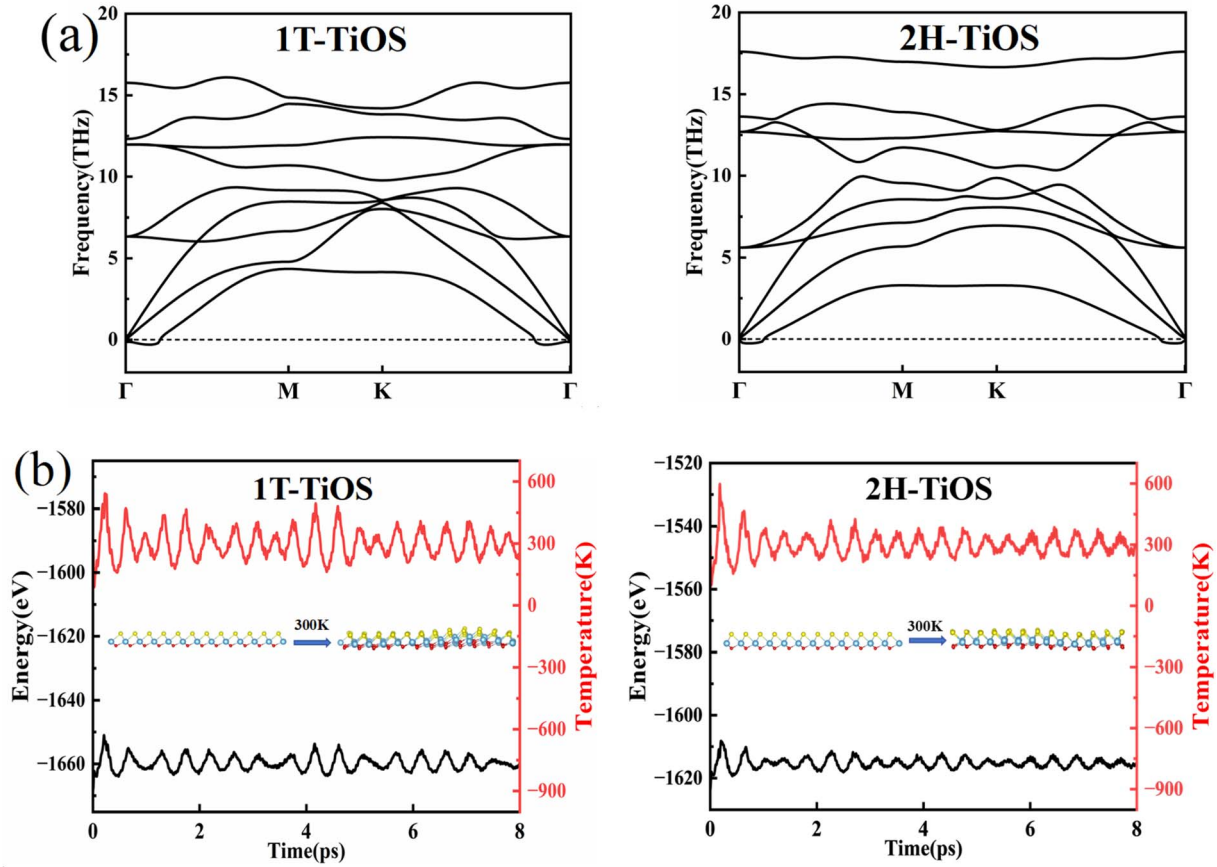

Fig. 2 (a) Phonon dispersion curves of Janus TiOS monolayers. (b) AIMD simulations of Janus TiOS monolayers at 300 K.

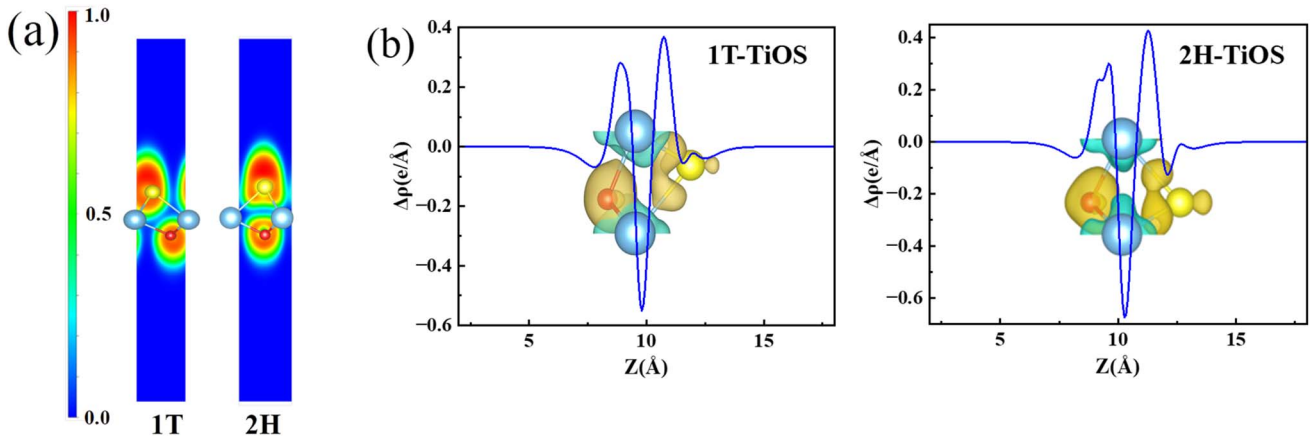

Fig. 3 (a) ELF of Janus TiOS monolayers. (b) Planar-averaged and 3D charge density differences of Janus TiOS monolayers. The blue and yellow isosurfaces represent electron depletion and accumulation, respectively, with an isosurface value of 0.01 e Å^{-3}.

has band gaps of 0.55 eV (PBE) and 1.27 eV (HSE06), while the 2H phase shows corresponding values of 0.62 eV (PBE) and 1.52 eV (HSE06). The HSE06 calculated band gap of 1.27 eV for the 1T phase agrees well with previously reported results, confirming the reliability of the present computational approach.[39] Notably, the band gaps of Janus TiOS monolayers are considerably smaller than those of bulk TiO_2 (3.2 eV)[46] and 1T-TiO_2 (3.29 eV),[9] yet they remain above the minimum energy required for photocatalytic water splitting (>1.23 eV).[47] These findings demonstrate that the band gaps can be effectively tuned through the construction of Janus structures, providing a feasible strategy for designing 2D materials with tailored optoelectronic properties.

To gain deeper insights into the electronic structure, the partial density of states (PDOS) of both phases is analyzed, as presented in Fig. 4(e)–(f). The PDOS analysis confirms that, in the 1T phase, the CBM is mainly derived from Ti 3d orbitals, while the VBM is primarily contributed by a combination of S 2p

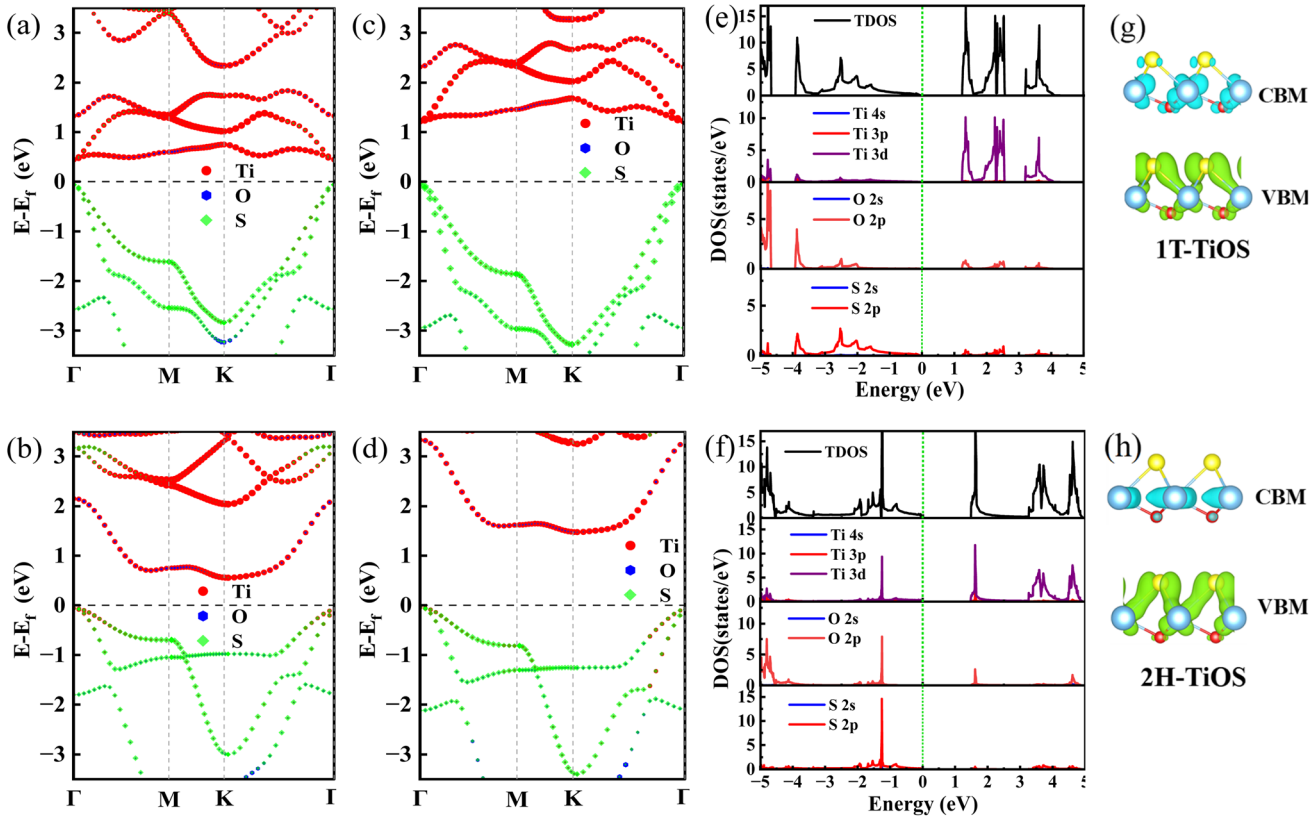

Fig. 4 Band structures of (a and b) 1T- and 2H-TiOS monolayers at the PBE level and (c and d) at the HSE06 level. PDOS of (e and f) 1T- and 2H-TiOS monolayers at the HSE06 level. (g and h) Side views of charge density distributions at the VBM (green) and CBM (blue) with an isosurface value of 0.02 e Å^{-3}.

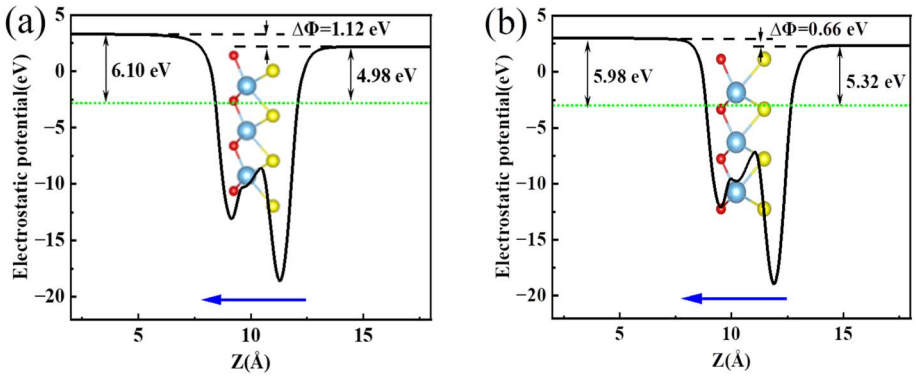

Fig. 5 Planar-average electrostatic potential of (a) 1T- and (b) 2H-TiOS monolayers.

and Ti 3d orbitals. Similarly, in the 2H phase, the CBM is dominated by Ti 3d states, and the VBM originates from the hybridization of S 2p and Ti 3d orbitals. These findings are consistent with the band structure analysis and provide a more comprehensive understanding of the electronic contributions.

Further visualization of the partial charge densities, as shown in Fig. 4(g)–(h), reveals the spatial distribution of the frontier electronic states. In both phases, the CBM is predominantly localized around the Ti atoms, whereas the VBM is primarily concentrated near the S atoms. This distinct spatial separation of photoexcited electrons and holes effectively suppresses their recombination kinetics, which is crucial for enhancing photocatalytic performance. The consistent trends observed in the band structure, density of states, and charge density analyses provide strong evidence for the intrinsic electronic characteristics of Janus TiOS monolayers.

The work function (Φ) is defined as $\Phi = E_v - E_f$, where E_v and E_f are the vacuum level and Fermi level, respectively. Fig. 5(a) and (b) show the calculated work functions and vacuum level differences of 1T- and 2H-TiOS monolayers after applying the dipole correction. A distinct surface potential difference ($\Delta\Phi$) arises from the electronegativity contrast between the S and O atoms on the upper and lower surfaces.[48] Because O is more electronegative than S, electrons are redistributed from the S layer toward the O layer, generating an intrinsic dipole oriented from the S-terminated surface to the O-terminated surface and a built-in electric field inside the monolayer. This internal field promotes the spatial separation and migration of photoexcited electrons and holes, thereby enhancing the charge-transport efficiency.[49]

3.3 Optical properties

Understanding the optical properties of 1T- and 2H-TiOS monolayers is crucial for a wide range of applications and experimental investigations. Fig. 6(a) presents the calculated optical absorption spectra, which display a pronounced absorption band in the visible-light region. In this range, the absorption coefficient of the 1T phase reaches 2.37×10^5 cm^{-1}, while that of the 2H phase is 1.95×10^5 cm^{-1}. With both values exceeding 10^5 cm^{-1}, Janus TiOS monolayers can be considered highly efficient in harvesting solar energy. By contrast, bulk TiO_2 exhibits almost no absorption in the visible region, and 1T-TiS_2 shows a much lower maximum absorption coefficient of only 4.19×10^4 cm^{-1}.[50,51] This comparison clearly demonstrates that Janus TiOS monolayers outperform their symmetric counterparts in visible-light absorption. Furthermore, their absorption coefficient rivals or even surpasses those of previously reported Janus 2D materials, such as MoSSe,[52] SnSSe,[53] PtSSe,[54] and ZrSSe.[55] The strong light absorption exhibited by Janus TiOS monolayers further underscores their significant potential as high performance photocatalysts.

Based on the band structure analysis, Janus TiOS monolayers exhibit suitable band gaps for photocatalytic water splitting. Besides having a suitable gap, a photocatalyst needs band edges

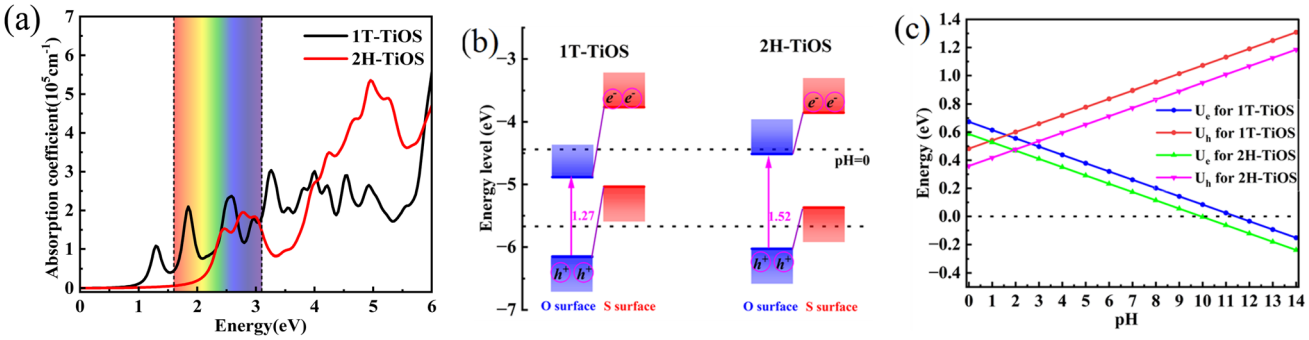

Fig. 6 (a) The optical absorption spectra of Janus TiOS monolayers computed using the HSE06 functional. (b) Band edge positions of Janus TiOS monolayers. (c) Water redox potential with pH.

Table 2 Elastic constants (C_{ij}), Young's modulus (Y), Poisson's ratio (ν) of Janus TiOS and typical 2D monolayers

Material	C_{11} (N m^{-1})	C_{12} (N m^{-1})	Y (N m^{-1})	ν
1T-TiOS	121.30	35.51	110.90	0.29
2H-TiOS	138.78	49.91	120.84	0.36
2H-TiO_2	173.7 (ref. 59)	75.7 (ref. 59)	141.7 (ref. 59)	0.44 (ref. 59)
2H-TiS_2	89.9 (ref. 59)	28.6 (ref. 59)	80.8 (ref. 59)	0.32 (ref. 59)
1T-MoS_2	132.7 (ref. 59)	33.0 (ref. 59)	124.5 (ref. 59)	0.25 (ref. 59)
2H-MoS_2	130,[60] 133.36 (ref. 61)	32,[60] 37.05 (ref. 61)	123.07,[61] 127.3 (ref. 62)	0.34,[60] 0.28 (ref. 61)
2H-MoO_2	232.92 (ref. 62)	84.67 (ref. 62)	202.1 (ref. 62)	0.36 (ref. 62)
1T-WS_2	146.5 (ref. 59)	31.8 (ref. 59)	139.6 (ref. 59)	0.22 (ref. 59)
2H-WS_2	144,[60] 148.47 (ref. 62)	31,[60] 31.20 (ref. 62)	141.9 (ref. 62)	0.36,[60] 0.21 (ref. 62)
2H-WO_2	261.2 (ref. 59)	87.8 (ref. 59)	231.7 (ref. 59)	0.34 (ref. 59)
Ti_2C	137 (ref. 63)	32 (ref. 63)	130 (ref. 63)	0.23,[63] 0.30 (ref. 64)
h-BN	291 (ref. 60)	62 (ref. 60)	271 (ref. 65)	0.211 (ref. 65)
Graphene	354 (ref. 66)	60 (ref. 66)	344 (ref. 66)	0.19,[67] 0.169 (ref. 66)
2H-CrSO	157.86 (ref. 68)	43.71 (ref. 68)	145.76 (ref. 68)	0.28 (ref. 68)
2H-WSO	196 (ref. 69)	52 (ref. 69)	182 (ref. 69)	0.27 (ref. 69)

aligned to water redox levels, with the VBM below the oxidation potential and the CBM above the reduction potential. Fig. 6(b) presents the band-edge alignment of Janus TiOS monolayers with respect to the dipole-corrected vacuum levels on their O- and S-terminated surfaces. When the band edges are referenced to the local vacuum level, the intrinsic HSE band gaps of both the 1T and 2H phases are preserved. However, the $\Delta\Phi$ between the two terminations gives rise to an intrinsic band bending, providing an effective means of band-edge modulation for enhanced photocatalytic activity.[56,57] At pH = 0, the VBM of both 1T- and 2H-TiOS on the O-terminated side lie below the water oxidation potential, whereas the CBM on the S-terminated side are located above the water reduction potential. This asymmetric band alignment enhances the oxidation driving force at the O-terminated surface and simultaneously strengthens the reduction driving force at the S-terminated surface.

In addition, the pH dependence of the driving forces for photoexcited electrons and holes is evaluated using the following equations:[58]

$$U_e = E_{CBM} - (0.059 \times pH - 4.44) \quad (2)$$

$$U_h = -E_{VBM} + (0.059 \times pH - 5.67) \quad (3)$$

where U_e and U_h represent the carrier potentials that determine the reducing and oxidizing driving capabilities of the system, respectively. When both U_e and U_h are positive, the photocatalyst is thermodynamically capable of driving overall water splitting, and larger magnitudes of U_e and U_h correspond to stronger driving forces for the water oxidation and reduction half-reactions.[58] As shown in Fig. 6(c), both TiOS monolayers exhibit sufficient driving forces of photoexcited electrons and holes to enable photocatalytic water splitting over a wide pH range (0–10), underscoring the remarkable photocatalytic potential of Janus TiOS monolayers for solar-driven water splitting.

3.4 Mechanical and piezoelectric properties

The mechanical properties of materials are crucial for assessing their suitability for practical applications. To evaluate the mechanical stability of 1T- and 2H-TiOS monolayers, we applied the Born–Huang criterion. First, we calculated their elastic constants (C_{ij}), from which key mechanical properties such as Young's modulus (Y), and Poisson's ratio (ν) were derived. The results are summarized in Table 2.

As shown in Table 2, $C_{11} > 0$ and $C_{11} > |C_{12}|$, which satisfies the structural stability criterion proposed by Born–Huang, indicating the mechanical stability of both 1T- and 2H-TiOS.[70] The Young's moduli of the 1T- and 2H-TiOS monolayers fall between those of TiO_2 and TiS_2.[59] Their stiffness is generally lower than that of Janus monolayers with a similar structural phase, such as 2H-CrSO and 2H-WSO, and also lower than that of many widely studied 2D materials, including Ti_2C, h-BN, graphene, representative transition-metal dichalcogenides (TMDCs) such as MoS_2 and WS_2, and transition-metal oxides (TMOs) such as MoO_2 and WO_2.[59–69] The Poisson's ratios of 1T- and 2H-TiOS monolayers are 0.29 and 0.36, respectively, falling within the range $0.25 < \nu < 0.5$, which indicates predominantly ionic bonding, consistent with the ELF analysis.[71] These values are slightly higher than those of Ti_2C, h-BN, and graphene, and comparable to those of other Janus monolayers such as WSO and CrSO, together with typical TMDCs and TMOs including MoS_2, WS_2, MoO_2, and WO_2.[59–69] Overall, owing to their moderate stiffness and favorable ductility, the Janus TiOS monolayers display exceptional mechanical adaptability, rendering them highly promising for strain-engineered modulation of optoelectronic properties.

Due to the lack of mirror symmetry, Janus TiOS monolayers exhibit strong in-plane and significantly weaker out-of-plane piezoelectric polarizations under uniaxial in-plane strain. The piezoelectric coefficients e_{11} and e_{31} are computed using DFT. The obtained e_{ij} values are then used to determine d_{11} and d_{31} through the following relationships:[24]

$$d_{11} = \frac{e_{11}}{(C_{11} - C_{12})} \quad (4)$$

$$d_{31} = \frac{e_{31}}{(C_{11} + C_{12})} \quad (5)$$

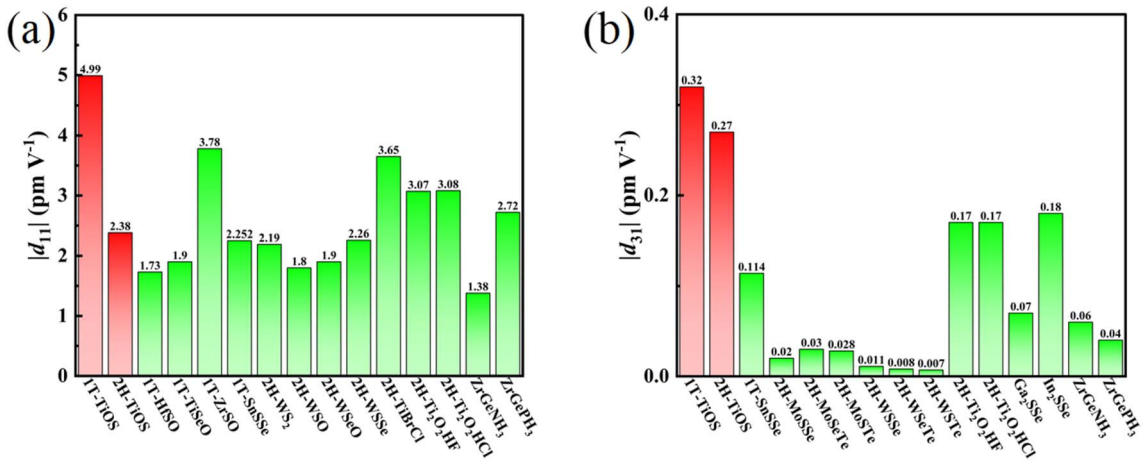

Fig. 7 Piezoelectric coefficients of Janus TiOS monolayers and other monolayers: (a) d_{11}, (b) d_{31}.

Fig. 7 summarizes the piezoelectric coefficients of Janus TiOS monolayers and compares them with those of other 2D materials. The calculated d_{11} value for 1T-TiOS is in good agreement with previously reported results.[39] As shown in Fig. 7(a), the in-plane piezoelectric response of 1T-TiOS exceeds that of other 1T counterparts, including HfSO, TiSeO, ZrSO, and SnSSe.[39,53] For the 2H phase, the in-plane coefficient is slightly smaller than that of other isostructural Ti-based Janus systems such as Ti_2O_2HF, Ti_2O_2HCl, and TiBrCl, but remains larger than those of WS_2, WSO, WSeO, WSSe, and $ZrGeNH_3$.[16,20,60,69,72,73] Meanwhile, Fig. 7(b) illustrates that the out-of-plane piezoelectric coefficients of 1T- and 2H-TiOS (0.32 pm V^{-1} and 0.27 pm V^{-1}, respectively) exceed those of Janus MoSSe, MoSeTe, MoSTe, WSSe, WSeTe, and WSTe by more than one order of magnitude. Notably, TiOS monolayers demonstrate stronger out-of-plane piezoelectric responses compared to numerous other reported Janus systems, such as Ti_2O_2HF, Ti_2O_2HCl, Ga_2SSe, In_2SSe, $ZrGeNH_3$, $ZrGePH_3$, and $ZrGeAsH_3$.[72–74] Overall, both 1T- and 2H-TiOS monolayers exhibit notable piezoelectric performance. The 1T phase, in particular, possesses higher piezoelectric coefficients and pronounced in-plane and out-of-plane responses, rendering it a promising material for integrated photocatalytic–piezoelectric applications.

4 Conclusion

In summary, the structural, electronic, optical, mechanical, and piezoelectric properties of 2D Janus TiOS monolayers (1T and 2H phases) were systematically investigated using first-principles calculations. Janus TiOS monolayers exhibit dynamic, thermal, and mechanical stability. Electronic structure analysis reveals that the 1T-TiOS monolayer behaves as a direct-bandgap semiconductor, while the 2H-TiOS monolayer exhibits an indirect bandgap. The calculated band gaps at the HSE06 level are 1.27 eV for the 1T phase and 1.52 eV for the 2H phase. Additionally, the CBM and VBM of both monolayers are primarily determined by distinct atomic orbital contributions. Both monolayers demonstrate strong optical absorption in the visible spectrum, and their band-edge positions span the water redox potentials over a wide pH range (0–10), making them promising candidates for photocatalytic water splitting. The favorable ductility of the materials is reflected in their Young's modulus and Poisson's ratio. Furthermore, the piezoelectric coefficients of the 1T-TiOS monolayer surpass those of the 2H phase, indicating superior piezoelectric performance. These findings highlight the significant application potential of both the 1T and 2H phases of TiOS in fields such as photocatalysis and piezoelectric devices. This work provides a solid theoretical foundation for the design and application of Janus TiOS monolayers.

Author contributions

Jing Tang: conceptualization, data curation, investigation, methodology, validation, writing – original draft, writing – review & editing. Kaimin Fan: conceptualization, funding acquisition, methodology, project administration, resources, writing – review & editing. Kun Wang: writing – review & editing.

Conflicts of interest

There are no conflicts of interest to declare.

Data availability

This study did not generate any new datasets. All data analyzed are from publicly available sources, as cited in the manuscript.

Acknowledgements

This work was supported by the Scientific Research Project of "Kunlun Elite Talents" Program of Qinghai Province, China (2025-QLGKLYCZX-022).

References

1 M. Humayun, F. Raziq, A. Khan and W. Luo, *Green Chem. Lett. Rev.*, 2018, **11**, 86–102.

2 T. L. Soundarya, T. Jayalakshmi, M. A. Alsaiari, M. Jalalah, A. Abate, F. A. Alharthi, N. Ahmad and G. Nagaraju, *Crystals*, 2022, **12**, 1133.
3 K. Lee, H. Yoon, C. Ahn, J. Park and S. Jeon, *Nanoscale*, 2019, **11**, 7025–7040.
4 S. Lettieri, M. Pavone, A. Fioravanti, L. Santamaria Amato and P. Maddalena, *Materials*, 2021, **14**, 1645.
5 V. T. T. Ho, D. H. Chau, K. Q. Bui, N. T. T. Nguyen, T. K. N. Tran, L. G. Bach and S. N. Truong, *Inorganics*, 2022, **10**, 29.
6 D. N. Shvalyuk, M. G. Shelyapina and I. A. Zvereva, *Results Chem.*, 2024, **7**, 101296.
7 J. Yang, Y.-L. Jiang, L.-J. Li, E. Muhire and M.-Z. Gao, *Nanoscale*, 2016, **8**, 8170–8177.
8 H. Zhu, X. Yang, M. Zhang, Q. Li and J. Yang, *Mater. Res. Bull.*, 2020, **125**, 110765.
9 I. Kim, G. Lee and M. Choi, *Phys. Rev. Mater.*, 2020, **4**, 094001.
10 F. A. Rasmussen and K. S. Thygesen, *J. Phys. Chem. C*, 2015, **119**, 13169–13183.
11 N. Anjum, M. Kashif, A. Shahzad, A. Rasheed and G. Ren, *ACS Omega*, 2024, **9**, 19848–19858.
12 M. Yagmurcukardes, C. Sevik and F. M. Peeters, *Phys. Rev. B*, 2019, **100**, 045415.
13 T. V. Vu, V. T. T. Vi, H. V. Phuc, A. I. Kartamyshev and N. N. Hieu, *Phys. Rev. B*, 2021, **104**, 115410.
14 N. N. Hieu, H. V. Phuc, A. I. Kartamyshev and T. V. Vu, *Phys. Rev. B*, 2022, **105**, 075402.
15 Y. Wang, Y. Tao, Q. Zhang, R. Huang, B. Gao, Z. Li, G. Li and N. Hu, *Solid State Commun.*, 2022, **354**, 114893.
16 Q. Yang, T. Zhang, C.-E. Hu, X.-R. Chen and H.-Y. Geng, *Phys. Chem. Chem. Phys.*, 2023, **25**, 274–285.
17 X. Lei, C. Ouyang and K. Huang, *Appl. Surf. Sci.*, 2021, **537**, 147919.
18 C. Xia, W. Xiong, J. Du, T. Wang, Y. Peng and J. Li, *Phys. Rev. B*, 2018, **98**, 165424.
19 H. Qu, S. Zhang, J. Cao, Z. Wu, Y. Chai, W. Li, L.-J. Li, W. Ren, X. Wang and H. Zeng, *Sci. Bull.*, 2024, **69**, 1427–1436.
20 L. Dong, J. Lou and V. B. Shenoy, *ACS Nano*, 2017, **11**, 8242–8248.
21 A.-Y. Lu, H. Zhu, J. Xiao, C.-P. Chuu, Y. Han, M.-H. Chiu, C.-C. Cheng, C.-W. Yang, K.-H. Wei, Y. Yang, Y. Wang, D. Sokaras, D. Nordlund, P. Yang, D. A. Muller, M.-Y. Chou, X. Zhang and L.-J. Li, *Nat. Nanotechnol.*, 2017, **12**, 744–749.
22 T. Zheng, Y.-C. Lin, Y. Yu, P. Valencia-Acuna, A. A. Puretzky, R. Torsi, C. Liu, I. N. Ivanov, G. Duscher, D. B. Geohegan, Z. Ni, K. Xiao and H. Zhao, *Nano Lett.*, 2021, **21**, 931–937.
23 A. Mogulkoc, Y. Mogulkoc, S. Jahangirov and E. Durgun, *J. Phys. Chem. C*, 2019, **123**, 29922–29931.
24 T.-T. Yan, G.-X. Zhou, X.-L. Jiang, X.-C. Qin and J. Li, *Phys. Chem. Chem. Phys.*, 2024, **26**, 23998–24007.
25 G. Kresse and J. Furthmüller, *Phys. Rev. B:Condens. Matter Mater. Phys.*, 1996, **54**, 11169–11186.
26 G. Kresse, *J. Non-Cryst. Solids*, 1995, **192**, 222–229.
27 G. Kresse and J. Furthmüller, *Comput. Mater. Sci.*, 1996, **6**, 15–50.
28 G. Kresse and D. Joubert, *Phys. Rev. B:Condens. Matter Mater. Phys.*, 1999, **59**, 1758–1775.
29 S. Grimme, J. Antony, S. Ehrlich and H. Krieg, *J. Chem. Phys.*, 2010, **132**, 154104.
30 J. P. Perdew, K. Burke and M. Ernzerhof, *Phys. Rev. Lett.*, 1997, **78**, 1396.
31 J. Heyd, G. E. Scuseria and M. Ernzerhof, *J. Chem. Phys.*, 2003, **118**, 8207–8215.
32 H. J. Monkhorst and J. D. Pack, *Phys. Rev. B*, 1976, **13**, 5188–5192.
33 A. Togo and I. Tanaka, *Scr. Mater.*, 2015, **108**, 1–5.
34 G. J. Martyna, M. L. Klein and M. Tuckerman, *J. Chem. Phys.*, 1992, **97**, 2635–2643.
35 K. Momma and F. Izumi, *J. Appl. Crystallogr.*, 2008, **41**, 653–658.
36 V. Wang, N. Xu, J.-C. Liu, G. Tang and W.-T. Geng, *Comput. Phys. Commun.*, 2021, **267**, 108033.
37 Y.-J. Xiang, S. Gao, C. Wang, H. Fang, X. Duan, Y.-F. Zheng and Y.-Y. Zhang, *Chin. Phys. B*, 2024, **33**, 087101.
38 P. Zhang, S. Fu, C. Pu, X. Tang and D. Zhou, *Chin. Phys. B*, 2025, **34**, 057103.
39 W. Chen, X. Hou, X. Shi and H. Pan, *ACS Appl. Mater. Interfaces*, 2018, **10**, 35289–35295.
40 J. Zhang, S. Jia, I. Kholmanov, L. Dong, D. Er, W. Chen, H. Guo, Z. Jin, V. B. Shenoy, L. Shi and J. Lou, *ACS Nano*, 2017, **11**, 8192–8198.
41 B. Özdamar, G. Özbal, M. N. Çınar, K. Sevim, G. Kurt, B. Kaya and H. Sevinçli, *Phys. Rev. B*, 2018, **98**, 045431.
42 N. L. P. Andrews, J. Z. Fan, R. L. Forward, M. C. Chen and H.-P. Loock, *Phys. Chem. Chem. Phys.*, 2017, **19**, 73–81.
43 C. Qi, C. Yan, Q. Li, T. Yang, S. Qiu and J. Cai, *J. Mater. Chem. C*, 2023, **11**, 3262–3274.
44 M. Mizuno, I. Tanaka and H. Adachi, *Phys. Rev. B:Condens. Matter Mater. Phys.*, 1999, **59**, 15033–15047.
45 B. Jiang, J. M. Zuo, N. Jiang, M. O'Keeffe and J. C. H. Spence, *Acta Crystallogr., Sect. A: Found. Crystallogr.*, 2003, **59**, 341–350.
46 D. O. Scanlon, C. W. Dunnill, J. Buckeridge, S. A. Shevlin, A. J. Logsdail, S. M. Woodley, C. R. A. Catlow, M. J. Powell, R. G. Palgrave, I. P. Parkin, G. W. Watson, T. W. Keal, P. Sherwood, A. Walsh and A. A. Sokol, *Nat. Mater.*, 2013, **12**, 798–801.
47 T. Jafari, E. Moharreri, A. Amin, R. Miao, W. Song and S. Suib, *Molecules*, 2016, **21**, 900.
48 T. Zhao, J. Chen, X. Wang and M. Yao, *Appl. Surf. Sci.*, 2021, **545**, 148968.
49 H. Ma, Z. Wang, W. Zhao, H. Ren, H. Zhu, Y. Chi and W. Guo, *J. Phys. Chem. Lett.*, 2022, **13**, 8484–8494.
50 F. Saidi, A. Mahmoudi, K. Laidi, T. Hidouri and S. Nasr, *Comput. Condens. Matter*, 2021, **28**, e00576.
51 H. Liu, L. Yang, Y. Zhao, S. Sun and X. Wei, *J. Supercond. Nov. Magn.*, 2024, **37**, 639–655.
52 X. Zuo, K. Chang, J. Zhao, Z. Xie, H. Tang, B. Li and Z. Chang, *J. Mater. Chem. A*, 2016, **4**, 51–58.
53 S.-D. Guo, X.-S. Guo, R.-Y. Han and Y. Deng, *Phys. Chem. Chem. Phys.*, 2019, **21**, 24620–24628.

54 R. Peng, Y. Ma, B. Huang and Y. Dai, *J. Mater. Chem. A*, 2019, **7**, 603–610.
55 T. V. Vu, H. D. Tong, D. P. Tran, N. T. T. Binh, C. V. Nguyen, H. V. Phuc, H. M. Do and N. N. Hieu, *RSC Adv.*, 2019, **9**, 41058–41065.
56 Z. Haman, M. Kibbou, N. Khossossi, E. Ouabida, P. Dey, I. Essaoudi and A. Ainane, *Int. J. Hydrogen Energy*, 2024, **68**, 566–574.
57 Y. Ji, M. Yang, H. Lin, T. Hou, L. Wang, Y. Li and S.-T. Lee, *J. Phys. Chem. C*, 2018, **122**, 3123–3129.
58 H. Zhang, C.-Q. Zhou and F.-S. Meng, *Solid State Commun.*, 2023, **370**, 115220.
59 M. M. Alyörük, Y. Aierken, D. Çakır, F. M. Peeters and C. Sevik, *J. Phys. Chem. C*, 2015, **119**, 23231–23237.
60 K.-A. N. Duerloo, M. T. Ong and E. J. Reed, *J. Phys. Chem. Lett.*, 2012, **3**, 2871–2876.
61 H. Sun, P. Agrawal and C. V. Singh, *Mater. Adv.*, 2021, **2**, 6631–6640.
62 F. Zeng, W.-B. Zhang and B.-Y. Tang, *Chin. Phys. B*, 2015, **24**, 097103.
63 S. Wang, J.-X. Li, Y.-L. Du and C. Cui, *Comput. Mater. Sci.*, 2014, **83**, 290–293.
64 Y.-C. Lu, C.-L. Ren, C.-Y. Wang, Y.-R. Yin, H. Han, W. Zhang and P. Huai, *Nucl. Sci. Technol.*, 2019, **30**, 172.
65 K. N. Kudin, G. E. Scuseria and B. I. Yakobson, *Phys. Rev. B:Condens. Matter Mater. Phys.*, 2001, **64**, 235406.
66 E. Cadelano, P. L. Palla, S. Giordano and L. Colombo, *Phys. Rev. B:Condens. Matter Mater. Phys.*, 2010, **82**, 235414.
67 A. Politano and G. Chiarello, *Nano Res.*, 2015, **8**, 1847–1856.
68 T. P. T. Linh, N. N. Hieu, H. V. Phuc, C. Q. Nguyen, P. T. Vinh, N. Q. Thai and N. V. Hieu, *RSC Adv.*, 2021, **11**, 39672–39679.
69 M. J. Varjovi, M. Yagmurcukardes, F. M. Peeters and E. Durgun, *Phys. Rev. B*, 2021, **103**, 195438.
70 F. Mouhat and F.-X. Coudert, *Phys. Rev. B:Condens. Matter Mater. Phys.*, 2014, **90**, 224104.
71 Y. Ö. Çiftci, *Can. J. Phys.*, 2016, **94**, 328–333.
72 J. Qiu and J. Liu, *Mater. Lett.*, 2024, **367**, 136620.
73 T. V. Vu, V. T. T. Vi, N. T. Hiep, K. V. Hoang, A. I. Kartamyshev, H. V. Phuc and N. N. Hieu, *RSC Adv.*, 2024, **14**, 21982–21990.
74 Y. Guo, S. Zhou, Y. Bai and J. Zhao, *Appl. Phys. Lett.*, 2017, **110**, 163102.